ISPRS Journal of Photogrammetry and Remote Sensing 109 (2015) 139–151

Contents lists available at ScienceDirect

ISPRS Journal of Photogrammetry and Remote Sensing

journal homepage: www.elsevier.com/locate/isprsjprs

Geometric integration of high-resolution satellite imagery and airborne LiDAR data for improved geopositioning accuracy in metropolitan areas

Bo Wu [a,*], Shengjun Tang [a,b,c], Qing Zhu [c], Kwan-yuen Tong [d], Han Hu [a,b,c], Guoyuan Li [e]

[a] Department of Land Surveying and Geo-Informatics, Hong Kong Polytechnic University, Hung Hom, Kowloon, Hong Kong
[b] State Key Laboratory of Information Engineering in Surveying Mapping and Remote Sensing, Wuhan University, Wuhan, PR China
[c] Faculty of Geosciences and Environmental Engineering, Southwest Jiaotong University, Chengdu, PR China
[d] Survey and Mapping Office, Lands Department, The Government of the Hong Kong Special Administrative Region, Hong Kong
[e] Satellite Surveying and Mapping Application Center, The National Administration of Surveying, Mapping and Geoinformation, Beijing, PR China

ARTICLE INFO

Article history:
Received 14 August 2014
Received in revised form 16 September 2015
Accepted 17 September 2015

Keywords:
High-resolution satellite imagery
Airborne LiDAR
Geopositioning accuracy
Geometric integration

ABSTRACT

High-resolution satellite imagery (HRSI) and airborne light detection and ranging (LiDAR) data are widely used for deriving 3D spatial information. However, the 3D spatial information derived from them in the same area can be inconsistent. Considering HRSI and LiDAR datasets taken from metropolitan areas as a case study, this paper presents a novel approach to the geometric integration of HRSI and LiDAR data to reduce their inconsistencies and improve their geopositioning accuracy. First, the influences of HRSI's individual rational polynomial coefficients (RPCs) on geopositioning accuracies are analyzed and the RPCs that dominate those accuracies are identified. The RPCs are then used as inputs in the geometric integration model together with the tie points identified in stereo images and LiDAR ground points. A local vertical constraint and a local horizontal constraint are also incorporated in the model to ensure vertical and horizontal consistency between the two datasets. The model improves the dominating RPCs and the ground coordinates of the LiDAR points, decreasing the inconsistencies between the two datasets and improving their geopositioning accuracy. Experiments were conducted using ZY-3 and Pleiades-1 imagery and the corresponding airborne LiDAR data in Hong Kong. The results verify that the geometric integration model effectively improves the geopositioning accuracies of both types of imagery and the LiDAR points. Furthermore, the model enables the full comparative and synergistic use of remote sensing imagery and laser scanning data collected from different platforms and sensors.

1. Introduction

High resolution satellite imagery (HRSI) has been widely used to derive 3D spatial information in a variety of applications such as building modeling (Baltsavias et al., 2001; Fraser et al., 2002), coastal mapping (Populus et al., 2001; Di et al., 2003a, 2003b) and disaster monitoring (Glenn et al., 2006; Kasai et al., 2009). Recently launched satellites such as GeoEye-1 and WorldView-2 from U.S. company DigitalGlobe and Pleiades-1 from the European company Airbus Defence and Space provide sub-meter geometric resolution for panchromatic imagery (Croft, 2008; Poli et al., 2013). The first Chinese civilian high-resolution mapping satellite, ZY-3, offers a 2.1-m resolution for panchromatic nadir imagery (Wang et al., 2014). HRSI is becoming more attractive in various applications due to its high quality imaging, short revisit time and lower cost. In the past decade, airborne laser scanning or light detection and ranging (LiDAR) technology has also been widely used to rapidly capture 3D surface data (point clouds) for a variety of applications (May and Toth, 2007). LiDAR has several advantages in that it offers very short delivery times that are much faster than traditional photogrammetric compilation, and provide extensive information that contains a wealth of detail due to the extraordinary number of points involved. HRSI and LiDAR are currently two major sources for obtaining 3D spatial information.

However, in circumstances where both HRSI and LiDAR data are available in a single area, it is not unusual to see inconsistencies in their derived 3D spatial information. For example, the differences between the 3D locations of objects (e.g., buildings) derived from LiDAR data in Hong Kong and those derived directly from the Pleiades-1 and ZY-3 imagery of the same objects range from several meters to over 20 m. Photogrammetric image processing

* Corresponding author. Tel.: +852 2766 4335; fax: +852 2330 2994.
E-mail address: bo.wu@polyu.edu.hk (B. Wu).

http://dx.doi.org/10.1016/j.isprsjprs.2015.09.006
0924-2716/

generally provides better accuracy in the horizontal direction than in the vertical direction (Li et al., 2007). Although LiDAR data is known to produce better vertical accuracy than horizontal accuracy (May and Toth, 2007; Qiao et al., 2010), the inconsistencies between the two datasets may be reduced via their geometric integration. This may improve the geopositioning accuracy of both datasets, which cannot be achieved when only the data from a single source are used.

The geometric integration of HRSI and LiDAR data has rarely been investigated. We developed an approach for the integrated processing of lunar satellite imagery and laser altimeter data to eliminate the possible discrepancies between the two datasets (Wu et al., 2011a, 2014). However, the lunar surface is relatively smooth, and it is more complicated to geometrically integrate HRSI and LiDAR data in metropolitan areas such as Hong Kong. Metropolitan areas present significant height variations due to their dense distributions of tall buildings and skyscrapers. A sudden change in an elevation or a slope makes the surface continuity constraint non-functional, but this also introduces new clues of using boundary features with significant elevation changes to provide constraints to the integration process.

This paper aims to geometrically integrate HRSI and LiDAR data in metropolitan areas to improve the geopositioning accuracy of both datasets. After presenting a literature review on the geopositioning accuracy analysis of HRSI and LiDAR data, we investigate the influence of HRSI's individual rational polynomial coefficients (RPCs) on geopositioning accuracy, and identify RPCs dominating that accuracy. A geometric integration model is then presented in detail for the integrated processing of HRSI and LiDAR data in metropolitan areas. The results of experimental analyses involving LiDAR data, ZY-3 imagery and Pleiades-1 imagery in Hong Kong are then used for experimental analysis. Finally, concluding remarks are presented and discussed.

2. Related work

The rational function model (RFM) is typically used to derive 3D spatial information from HRSI. It involves a mathematical fitting of the rigorous sensor model using polynomials that contain RPCs. Third-order polynomials usually consist of 78 RPCs, which the image supplier provides as image metadata (Li et al., 2007; Habib et al., 2007). Establishing the geopositioning accuracy of HRSI directly from RPCs depends on the quality of the HRSI's orbital navigation and stability. For example, ground coordinates derived from the RPCs of the IKONOS (Geo Level) stereo product have exhibited a systematic horizontal shift (16–25 m) (Dial and Grodecki, 2002; Li et al., 2007, 2008). The typical QuickBird stereo (Basic Level) imagery has exhibited a similar shift of 23 m (Qiao et al., 2010). Fraser and Ravanbakhsh (2009) reported that systematic errors of about 2.5 m in horizontal and 7.6 m in height resulted from a direct space intersection when RPCs were used for a GeoEye-1 stereo image pair covering the Hobart HRSI test field in Hobart, Tasmania, Australia. This type of error is mainly caused by the possible biases within the RPCs, and can be removed or lessened by bias-correction models in either image or object space through a few good-quality ground control points (GCPs). Di et al. (2003a, 2003b) used a 3D affine transformation model to refine the RPC-derived ground coordinates of IKONOS images and achieved an accuracy of 1.5 m in planimetry and 1.6 m in height. Wang et al. (2005) tested different bias-correction models including translation, scale and translation, affine, and second-order polynomial models using IKONOS and QuickBird imagery. Their results indicated that meter lever accuracy can be obtained using an appropriate model and GCPs. Fraser and Hanley (2005), Toutin (2006), Habib et al. (2007) and Fraser and Ravanbakhsh (2009) reported similar results. Instead of adding corrections in image or object space, Tong et al. (2010) presented a method to directly modify and regenerate the RPCs based on bias-correction models for a stereo pair of QuickBird imagery in Shanghai, China. The results indicated the existence of high-order error signals in the original RPCs. Sub-meter accuracy can be achieved according to their approach with sufficient and appropriate GCPs. The direct regeneration of RPCs enables the convenient processing of HRSI through commercial photogrammetric software. However, their method requires a large number of GCPs and may arrive at unstable solutions given the large number of RPCs (78) involved.

The geopositioning accuracy of LiDAR data is related to the accuracy of the navigation solution, boresight misalignment angles, ranging and scan angle accuracy, and laser beam divergence (May and Toth, 2007). In the first few years of LiDAR mapping development, most providers quoted root mean square error (RMSE) accuracies of 15 cm. In fact, such accuracy can only be obtained in ideal situations (Hodgson et al., 2003). Bowen and Waltermire (2002) examined the errors of the LiDAR data collected in Richland County, South Carolina, and their results showed that the horizontal error of LiDAR points is typically large (a RMSE of about 120 cm). Xhardé et al. (2006) analyzed LiDAR data collected on the south coast of the Gaspé Peninsula, Canada in 2003 and 2004, and reported that the RMSEs were about 54 cm in horizontal and about 16.5 cm in vertical. Other research has demonstrated LiDAR data range accuracies for large-scale mapping applications at RMSEs from 26 to 153 cm (Adams and Chandler, 2002; Hodgson et al., 2003). The research has seldom addressed improving the accuracy of LiDAR data. Csanyi and Toth (2007) investigated the use of LiDAR-specific ground control targets to improve data accuracy. The test results they obtained from two flights showed that specifically designed LiDAR targets improved the centimeter-level accuracy of the final LiDAR product. However, the improvement mainly relied on specifically designed ground control targets. In recent years, the improving capabilities of direct geo-referencing technology (GNSS/INS) are having a positive impact on the accuracy of the LiDAR data. Habib (2008) reported an accuracy of 50 cm in horizontal and 15 cm in vertical for the LiDAR data collected using an OPTECH ALTM 2070 system from a flying altitude of 975 m, and the accuracy was further improved by applying several internal and external quality control means. Hladik and Alber (2012) presented a method to improve the LiDAR data based on high accuracy RTK observations, which reduced the overall mean error from about 100 cm to 10 cm. The ASPRS positional accuracy standards for digital geospatial data listed the expected horizontal errors (RMSE) for LiDAR data ranging from 13.1 cm at a flying altitude of 500 m to 67.6 cm at an altitude of 5 km (ASPRS, 2014).

Most research related to the integrated processing of HRSI and LiDAR data has concentrated on enhanced feature extraction, in which the elevation information provided by the LiDAR data is used to support the extraction of features from the imagery (Teo and Chen, 2004; Sohn and Dowman, 2007). St-Onge et al. (2008) and Steinmann et al. (2013) investigated the methods of assessing the accuracy of the forest height and biomass using satellite images and LiDAR data. Stal et al. (2013) presented a method of integrating aerial images and LiDAR data for 3D change detection in urban areas. A digital surface model (DSM) extracted from a stereo aerial images acquired in 2000 was compared with a DSM derived from LiDAR data collected in 2009 to obtain the information of 3D building changes. In the planetary mapping community, several endeavors have been made to geometrically integrate satellite imagery and laser altimetry data. Anderson and Parker (2002) investigated the registration between the imagery and laser altimeter data collected by the Mars orbiter camera (MOC) and Mars orbiter laser altimeter (MOLA), which were both onboard

the Mars Global Surveyor (MGS). Yoon and Shan (2005) presented a combined adjustment method to process MOC imagery and MOLA data and reported that the large mis-registration between the two datasets could be reduced to a certain extent. Spiegel (2007) presented a method for the co-registration of high resolution stereo camera (HRSC) images and MOLA data. Di et al. (2012) studied the co-registration of Chang'E-1 stereo images and laser altimeter data in the Sinus Iridum area on the Moon. An iterative closest point (ICP) algorithm was used to register the 3D points derived from the stereo images to the laser altimeter points, from which the image orientation parameters were refined to co-register the images and laser altimeter data. However, this method treated the Chang'E-1 laser altimeter data as the absolute controls, and the accuracy of the final generated topographic information depended on the data. Wu et al. (2011a) proposed integrating the Chang'E-1 imagery and laser altimeter data for lunar topographic mapping through a combined adjustment approach, in which the Chang'E-1 laser altimeter points, orientation parameters of the Chang'E-1 images and tie points collected from the stereo Chang'E-1 images were processed and adjusted to export the refined image orientation parameters and improved laser ground points. This approach eliminated the inconsistencies between the imagery and laser altimeter data and allowed precise lunar topographic information to be generated. The approach was further improved for the integrated processing of cross-mission and cross-sensor lunar image networks and laser altimeter data (Wu et al., 2014). However, the previous developments cannot be directly used for the geometric integration of HRSI and LiDAR data in metropolitan areas. These areas present significant variations in height and surface smoothness, and differ significantly from the surfaces on Mars and the Moon. Therefore, we further improved the method by incorporating new considerations and constraints to enable the effective integration of HRSI and LiDAR data while improving the geopositioning accuracy of both datasets.

Compared with previous works, this paper presents the following novel findings. First, the influence of individual RPCs of HRSI on geopositioning accuracy is analyzed in detail for the first time, and only those RPCs dominating the geopositioning accuracy are involved in the following geometric integration process. Second, a new horizontal constraint specifically designed for datasets in metropolitan areas is incorporated into the geometric integration model. Third, the geometric integration improves the geopositioning accuracy of both the HRSI and LiDAR data, which is unique.

3. Influence of individual RPCs of HRSI on geopositioning accuracy

HRSI normally uses an RFM to derive 3D spatial information. This model defines the relationship from a point in the image space to a point in the object space. The following equation is an example of the RFM:

$$l = \frac{N_1(P,L,H)}{N_2(P,L,H)} = \frac{(1PLH \ldots LH^2H^3)(a_1a_2a_3a_4 \ldots a_{19}a_{20})^T}{(1PLH \ldots LH^2H^3)(b_1b_2b_3b_4 \ldots b_{19}b_{20})^T}$$

$$s = \frac{N_3(P,L,H)}{N_4(P,L,H)} = \frac{(1PLH \ldots LH^2H^3)(c_1c_2c_3c_4 \ldots c_{19}c_{20})^T}{(1PLH \ldots LH^2H^3)(d_1d_2d_3d_4 \ldots d_{19}d_{20})^T} \quad (1)$$

where (l, s) are the image coordinates and (P, L, H) are the object coordinates (latitude, longitude and height) in a geographic reference system. To stabilize the calculation, the image and object coordinates are normalized to $(-1, 1)$ based on the regularization parameters. $a_i (i = 1–20)$, $b_i (i = 1–20)$, $c_i (i = 1–20)$ and $d_i (i = 1–20)$ are the RPCs defining the RFM. Although an image has 80 RPCs in total, b_1 and d_1 are normally set at 1, which lowers the number to 78 in most cases. The image supplier provides both the RPCs and regularization parameters in the image metadata.

Due to the previously mentioned problems, there are unavoidable errors at different levels and discrepancies between the RPC-derived coordinates and ground truth in the original RPCs provided by the image supplier. Most of previous research has used bias-correction methods in either image or object space to improve geopositioning accuracy, and the original RPCs remain unchanged. These methods adjust the entire image coverage as a whole through transformations in image space or object space, which derive from the actual situation that different adjustments may need to be applied to different local regions in the image. For example, Qiao et al. (2010) reported that in metropolitan areas the bias-correction method with GCPs on the ground is not sufficient to eliminate the biases associated with the local regions of tall buildings. In addition, the bias-correction methods require special data-processing software or programs. An alternative approach is to directly modify and regenerate the RPCs through geometric calculation such as the method presented in the next section, which has the potential to provide better geopositioning accuracy through direct adjustment to the geometric model of HRSI and enables its convenient processing through commercial photogrammetric software.

However, a geometric solution for calculating and regenerating RPCs may encounter over-parameterization and instability because there are 78 RPCs involved. Instead of regenerating all 78 RPCs, this paper intends to examine the individual RPCs and tries to identify those dominate the geopositioning accuracy. Based on mean–variance theory, the following method is developed and verified using ZY-3 and Pleiades-1 imagery in Hong Kong (details of the imagery can be found in the experimental analysis section).

(1) Dozens of evenly distributed tie points are identified from the stereo images of the two datasets through a reliable image matching algorithm (Wu et al., 2011b, 2012). The tie points are in sub-pixel precision and they are manually checked to ensure the reliability.
(2) The 3D coordinates of those tie points are obtained through space intersection based on Eq. (1) using the original RPCs.
(3) For each RPC in which R belongs to (a_1–a_{20}, b_2–b_{20}, c_1–c_{20} and d_2–d_{20}, where b_1 and d_1 are equal to 1), a change interval of $0.5R$ is added to R until it reaches $200R$, and a change interval of $-0.5R$ is added to R until it reaches $-200R$, while the other RPCs remain the same. Eight hundred new sets of 3D coordinates for the tie points are then calculated, in addition to the variances of those coordinates.
(4) The variances in horizontal and vertical direction are obtained and plotted for each RPC in each image.

Fig. 1 shows the results for the ZY-3 imagery. In each chart, the horizontal variances for each RPC are illustrated with a black line, and the values correspond with the left vertical axis. The vertical variances for each RPC are illustrated with a gray line, and the values correspond with the right vertical axis. As Fig. 1 shows, the variances in both horizontal and vertical directions for the first several RPCs in each category are significantly greater than those of the other RPCs, indicating that these several RPCs dominate the geopositioning accuracy and that changes made to the other RPCs would not significantly influence the geopositioning accuracy. This trend is very consistent between the ZY-3 forward- and backward-looking images, as shown in Fig. 1(a) and (b), respectively.

Fig. 2 shows the results for the Pleiades-1 imagery. The results are quite consistent with those of the ZY-3 imagery. Once again, the first several RPCs in each category dominate the geopositioning accuracy. There are small variations in a_9 and c_9 of the Pleiades-1 forward-looking imagery, and in b_9 and b_{10} of the Pleiades-1

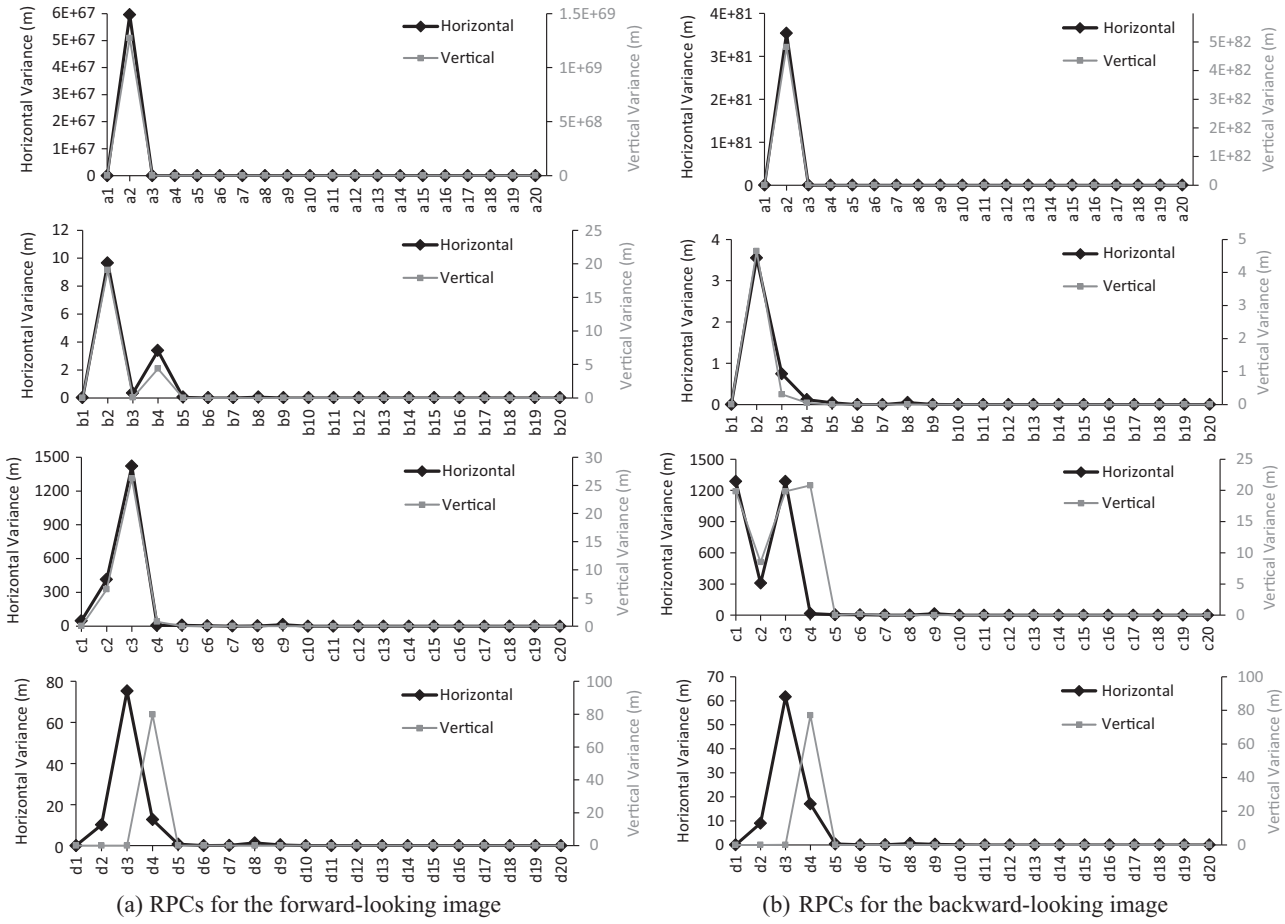

(a) RPCs for the forward-looking image (b) RPCs for the backward-looking image

Fig. 1. Variances of geopositioning accuracies in the horizontal and vertical directions in relation to the different RPCs of the ZY-3 imagery.

backward-looking imagery. However, these variances are negligible compared with those resulting from the first several RPCs.

We tested another set of IKONOS images (1-m resolution) collected at Tampa Bay, Florida in 2007, and the findings also show that the first several RPCs in each category dominate the geopositioning accuracy. This tendency may be related to the physical mechanism involved in determining the RPCs from the rigorous sensor model and the characteristics of the third-order polynomials in the RFM. Nevertheless, it makes these dominating RPCs the focus when improvements to geopositioning accuracy are considered. According to the results from both the ZY-3 and Pleiades-1 imagery, the first five RPCs in each category, including a_1–a_5, b_1–b_5, c_1–c_5 and d_1–d_5 (18 RPCs in total, as b_1 and d_1 are equal to 1) dominate the geopositioning accuracy of the RPCs and are used in the following geometric integration to improve that accuracy.

4. Geometric Integration of HRSI and LiDAR Data

4.1. Overview of the approach

The geometric integration model integrates HRSI and LiDAR data according to a rigid mathematical method. Tie points are obtained on the image pair through automatic image matching algorithms (Wu et al., 2011b, 2012). A selection strategy is then applied to identify the tie points that satisfy the integration process and are evenly distributed throughout the images. The ground coordinates of the tie points can be derived from the space intersection based on Eq. (1) using the original RPCs in the images. There may be discrepancies between the RPC-derived ground coordinates of the tie points and their corresponding ground truth. Based on Eq. (1), the LiDAR points can be back-projected to the stereo images using the original RPCs. Due to the RPC biases, the back-projected image points of a single LiDAR point may not match in terms of their textural features in the stereo images. The aim of the proposed geometric integration model is to eliminate or lessen these discrepancies and therefore improve the geopositioning accuracy of both the HRSI and LiDAR data.

In the model, the original dominating RPCs, tie points, tie point ground coordinates, LiDAR ground points and back-projected image coordinates of the LiDAR points are observables. Two constraints are incorporated into the model. First, the local vertical constraint is used to ensure vertical inter-consistency between the ground points of the tie points and neighboring LiDAR points. Second, the local horizontal constraint is used to ensure horizontal inter-consistency between the two parties. The geometric integration model ultimately improves the dominating RPCs and LiDAR point ground coordinates, decreasing the inconsistencies between the HRSI and LiDAR data and improving the geopositioning accuracy of both datasets in turn. The framework of the geometric integration approach is shown in Fig. 3.

4.2. Geometric integration model

After the linearization of Eq. (1), the geometric integration model of the HRSI and LiDAR data can be represented in matrix form as follows:

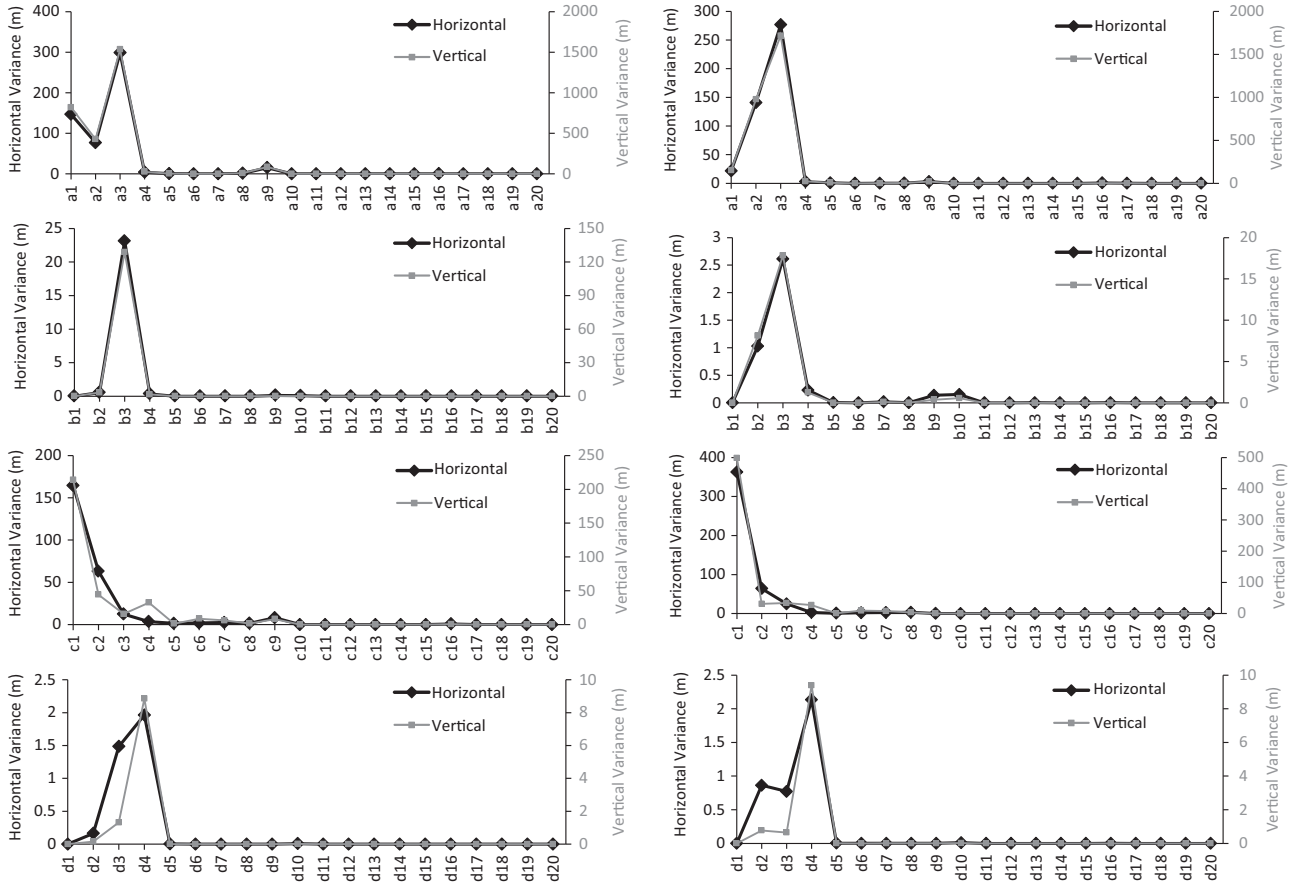

Fig. 2. Variances of geopositioning accuracies in the horizontal and vertical directions in relation to different RPCs for the Pleiades-1 imagery.

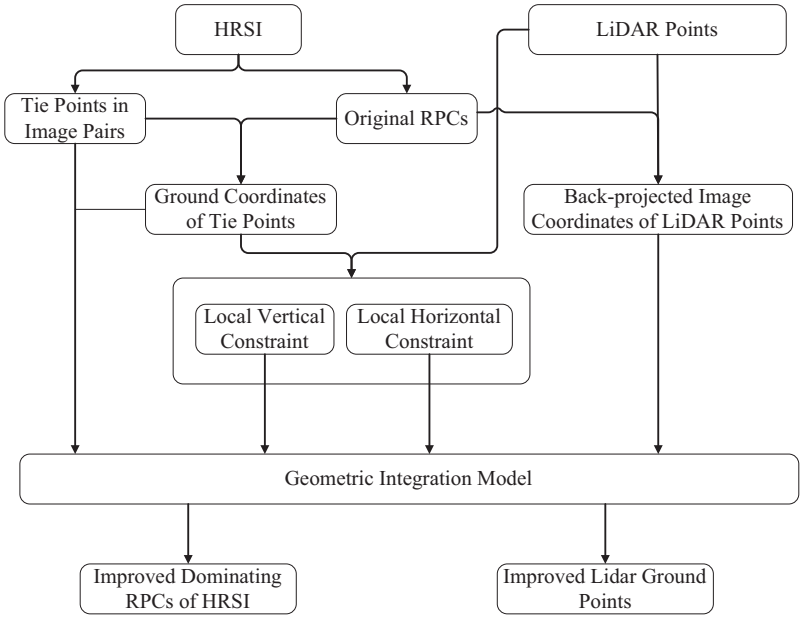

Fig. 3. Framework of the geometric integration model for HRSI and LiDAR data.

$$\begin{aligned} V_1 &= AX_1 - L_1, & P_1 \\ V_2 &= AX_1 + BX_2 - L_2, & P_2 \\ V_3 &= CX_3 - L_3, & P_3 \\ V_4 &= DX_4 - L_4, & P_4 \end{aligned} \tag{2}$$

The first observation equation relates to the dominating RPCs of the images. X_1 is the vector of corrections for the dominating RPCs. The RPCs in the denominators of Eq. (1) produce ill conditions in the error matrix, and the matrix of the normal equation may become singular. In general, the L-curve (Neumaier, 1998; Tao and Hu, 2001) is the best approach for solving the problem of an ill-conditioned matrix and is applied here.

The second observation equation is for the LiDAR points. X_2 is the vector of corrections to the ground coordinates of the LiDAR points. The back-projected image coordinates of the LiDAR points are not necessarily homologous points that represent the same texture on the stereo image, as there are inconsistencies between the two datasets. These points can be corrected in the integration process. Proper weights should be attached to the observation equation when calculating the LiDAR point corrections.

The third observation equation is a pseudo-observation related to the local vertical constraint in the integration model, which constrains the ground positions of the tie points to a local surface determined by the adjacent LiDAR points. X_3 is the vector of corrections to the elevations of the tie point ground positions. The fourth observation equation is a pseudo-observation related to the local horizontal constraint in the integration model, which is designed to lessen the inconsistencies between the tie and LiDAR point ground coordinates in the horizontal direction. X_4 is the vector of corrections to the horizontal coordinates (longitude and latitude) of the tie point ground positions. These two types of constraints are detailed in the following sections.

In the four observation equations in Eq. (2), P_1, P_2, P_3 and P_4 are the weights of each observation equation. The coefficient matrix A, B, C and D contains partial derivatives of the parameters to be corrected in each observation equation. The equations are solved iteratively based on a least squares approach to obtain a convergent solution.

4.3. Tie points determination

Two types of tie points are used in the geometric integration approach: vertical and horizontal. They are interactively selected from the results of an antecedent image matching process (Wu et al., 2011b, 2012). Fig. 4 illustrates the distribution patterns of the horizontal and vertical tie points.

As shown in Fig. 4, the vertical tie points are identified in the image regions with flat and smooth topographic features, such as playgrounds or grasslands. There are no sudden changes in height in these regions. These vertical tie points are used in the local vertical constraint to decrease the height differences between the HRSI and LiDAR datasets. The horizontal tie points are identified in the image regions with sharp topographic changes, such as building corners. For the purpose of establishing correspondences between the horizontal tie points on the images and those in the LiDAR data, a 3D surface with a grid resolution of 20 cm is interpolated from the original LiDAR point cloud, and the corresponding building corners are manually identified from the reconstructed 3D surface referring to the images. To ensure the reliability of the horizontal tie points, only those buildings with distinct boundaries are involved. These horizontal tie points are used in the local horizontal constraint to lessen the horizontal inconsistencies between the HRSI and LiDAR datasets. The process requires dozens of horizontal and vertical tie points evenly distributed throughout the image area.

4.4. Constraints in the geometric integration model

4.4.1. Local vertical constraint

Although metropolitan areas feature dense populations of tall buildings, they also include plenty of open spaces such as grasslands and playgrounds. The terrain fluctuations are continuous and smooth in these regions, enabling the use of a local vertical constraint during geometric integration, which was also applied in the lunar mapping in previous research (Wu et al., 2011a, 2014).

For the local vertical constraint, the height H of the ground point of the vertical tie point derived using the image RPCs should be consistent with a local surface determined by the nearby LiDAR points. A searching window centered at the horizontal location of the ground point of the vertical tie point with a size of a predefined value (e.g., 5 m for the Pleiades-1 imagery and 15 m for the ZY-3 imagery, depending on the image resolution and quality of the original RPCs) is constructed. All of the LiDAR points in this searching window are selected. Statistical analysis of the heights of the LiDAR points is conducted, and the points with heights three times greater than the standard deviation in the searching window are filtered out. These points may represent the LiDAR points belonging to the nearby buildings that are close to the vertical tie points. A local surface is fitted from the remaining LiDAR points, and a bilinear interpolation approach is used to interpolate another height H' for the vertical tie point from the local surface based on the horizontal location of its ground point. According to the third observation in Eq. (2), the difference between H and H' should approach 0.

Given this local vertical constraint, an improved accuracy in the vertical direction of the HRSI can be expected, as LiDAR data are normally very accurate in that direction. This is verified by the experimental results described in the next section. The involvement of a local vertical constraint also makes the geometric integration model solutions easy to converge.

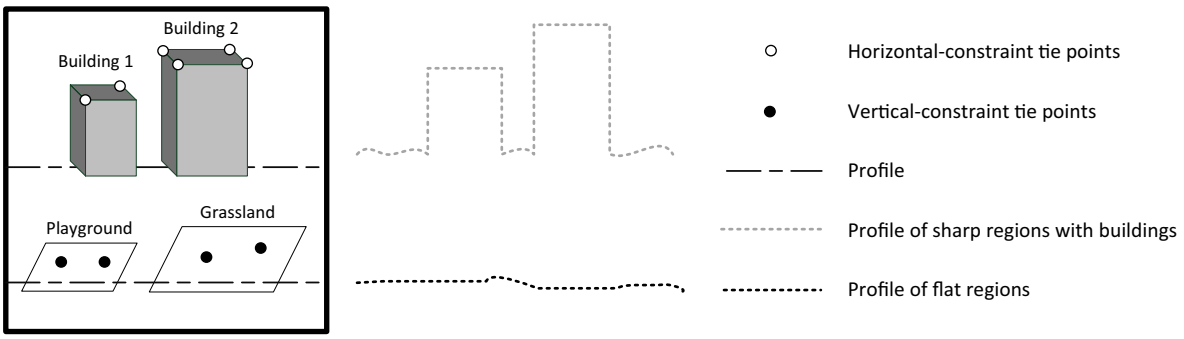

Fig. 4. Selection of horizontal and vertical tie points based on topographic features.

4.4.2. Local horizontal constraint

By incorporating the aforementioned local vertical constraint, the inconsistencies in height between the HRSI and the LiDAR data can be reduced. However, this local vertical constraint cannot lessen the inconsistencies in horizontal direction between the two datasets. A local horizontal constraint is therefore developed for this purpose.

The local horizontal constraint uses horizontal tie points identified on the stereo images as described previously. In metropolitan areas, the presence of tall buildings makes it easy to identify these horizontal tie points in both the HRSI and LiDAR data. However, only the horizontal information of the tie points in the imagery and those correspondingly extracted from the LiDAR data are used in the local horizontal constraint for two reasons. First, in the LiDAR data, although the horizontal locations of the building boundaries can be extracted accurately, the exact heights of the building boundaries are difficult to determine from the point clouds due to the drastic fluctuations in height around the building boundaries. Second, it is difficult to determine the height of the horizontal tie points from the HRSI and LiDAR data because the points are located along the building boundaries. Any small disturbance in the image coordinate or LiDAR point measurements would result in significant height determination errors. Therefore, the height information is discarded from this local horizontal constraint.

For the local horizontal constraint, the building boundary derived using the image RPCs should be consistent with that derived from the LiDAR data in horizontal. Fig. 5 illustrates the local horizontal constraint. The polygon in black is the building boundary extracted from the LiDAR data. The longitude and latitude coordinates of its corners n_1, n_2, n_3 and n_4 can be derived from the LiDAR data. The polygon in gray is the building boundary determined from the horizontal tie points in the images based on the RPCs. The longitude and latitude coordinates of its corners N_1, N_2, N_3 and N_4 can be calculated. According to the fourth observation in Eq. (2), the sum of the distances between n_1 and N_1, n_2 and N_2, n_3 and N_3, and n_4 and N_4 should approach 0.

It should be noted that the horizontal adjustment made to the HRSI or LiDAR data depends on the original accuracy of the datasets. This adjustment can be controlled based on the corresponding weights of the datasets. Large weight should be given to the more accurate dataset so that it is adjusted only slightly, and smaller weight should be given to the less accurate dataset so that it receives a greater adjustment.

4.5. Weight determination

In the geometric integration model of Eq. (2), the weights P_1, P_2, P_3 and P_4 represent the respective contributions of the observations. They are generally determined by the *a priori* standard deviation for each type of observation. For the experimental results presented in this paper, the weights are determined as follows.

For the first observation equation related to the RPCs of HRSI, the weight P_1 depends on the initial accuracy of the RPCs. Because the image supplier provides no such direct information about the accuracy of the RPCs, the ground coordinates of the tie points derived from the space intersection are compared using the RPCs and those identified from the LiDAR data. P_1 is assigned to be $1/\sqrt{\sigma_P^2+\sigma_L^2+\sigma_H^2}$, of which σ_P, σ_L and σ_H are the differences between the two datasets in the longitude, latitude and height directions, respectively. This method guarantees that the more accurate RPCs are given greater weight and therefore contribute more to the geometric integration process.

P_2 in the second observation equation is related to the LiDAR points. The vertical and horizontal accuracies of the LiDAR points

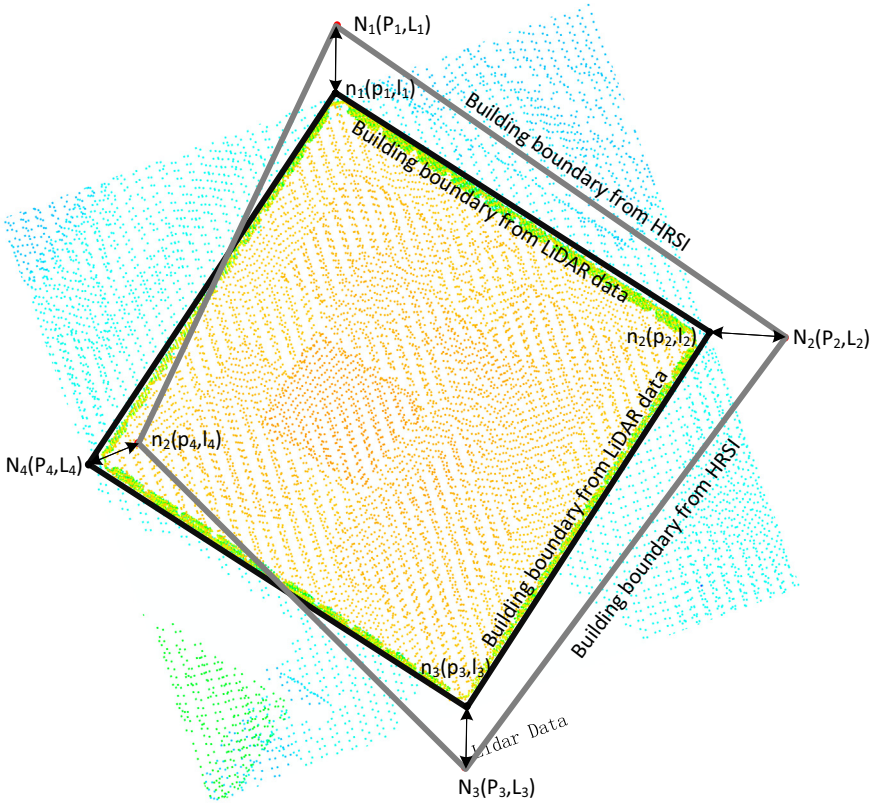

Fig. 5. Illustration of the local horizontal constraint.

are different, and normally the former are superior to the latter. Therefore, different weights are set in P_2 for the horizontal coordinates and heights of the LiDAR points in reference to the accuracy information provided in the metafile of the LiDAR data. The weight P_3 in the third observation equation relating to the local vertical constraint is set at a very large value because the LiDAR data is normally very accurate in the vertical direction, and the height information of the LiDAR data should be used to refine the height information from the HRSI. The weight P_4 in the last observation equation relates to the local horizontal constraint. A ratio of P_3 is assigned to P_4 and determined by the vertical accuracy (*a priori* standard deviation) of the LiDAR data divided by its horizontal accuracy.

To obtain the optimum weight for each observation, an iteration process is introduced in the actual experiments. For the weights P_1, P_2, P_3, and P_4 determined based on the aforementioned principles, a change interval of $0.1P_i$ ($i = 1, 2, 3, 4$) is applied to P_i until it reaches $0.5P_i$ and $1.5P_i$, and the optimum weights are obtained in the iteration process when the best geopositioning accuracies are achieved.

5. Experimental analysis

5.1. Datasets

The datasets used in the following experimental analysis include ZY-3 and Pleiades-1 images and LiDAR data covering Hong Kong Island and part of the Kowloon Peninsula. There are vast amounts of skyscrapers and tall buildings densely distributed across these regions. The ZY-3 imagery covers a region of W113.81–114.42° and N22.03–22.63°N. The Pleiades-1 imagery covers a region of W114.05–114.26° and N22.23–22.30°N. The detailed parameters of the ZY-3 and Pleiades-1 images are listed in Table 1, and the study areas in the ZY-3 and Pleiades-1 images are shown in Figs. 6 and 7, respectively.

The airborne LiDAR data were collected between December 1 2010 and January 8 2011, and covered Hong Kong Island and the Kowloon Peninsula. Fig. 8 shows a 3D view of part of the LiDAR points in Hong Kong Island and an intensity map of the LiDAR data showing its entire coverage.

Table 1
Parameters of the HRSI used in the experiments.

Items	ZY-3		Pleiades-1	
	Forward-looking image	Backward-looking image	Forward-looking image	Backward-looking image
Acquisition date	2013/3/8	2013/3/8	2013/3/4	2013/3/4
Acquisition time	11:11	11:12	7:33	7:03
Image size	16,306 * 16384 pixels	16,306 * 16384 pixels	15,173 * 20,542 pixels	15,374 * 20,628 pixels
Resolution (m)	3.3676 m/pixel	3.3795 m/pixel	0.5045 m/pixel	0.5015 m/pixel
Image swath	50 km	50 km	20 km	20 km
Convergence angle	44°		14.8°	

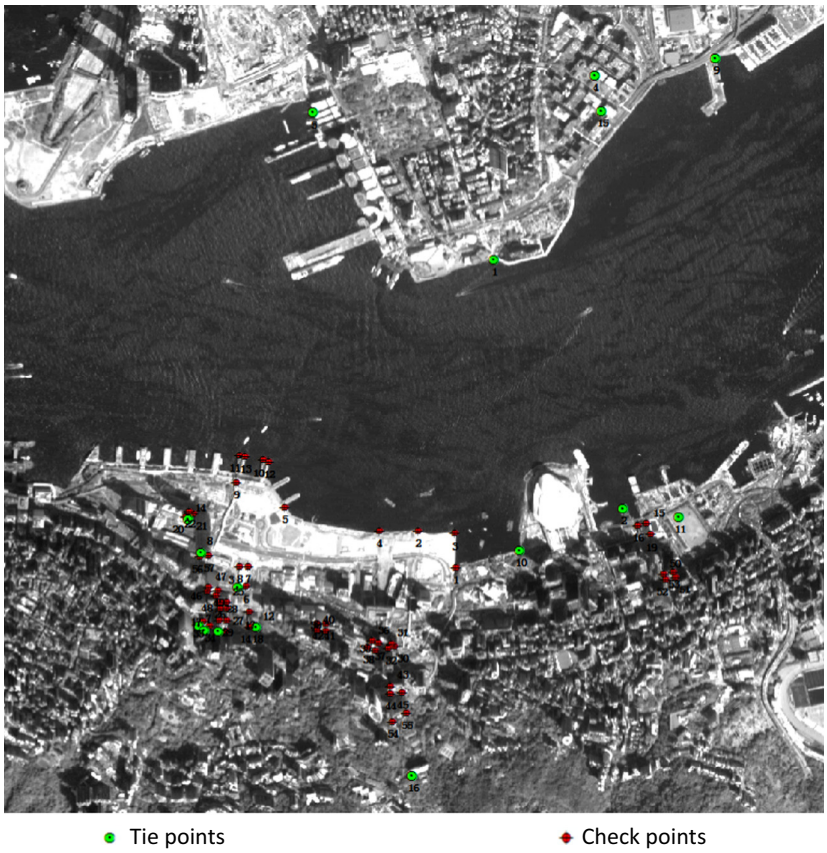

Fig. 6. The ZY-3 image of the study area, marked with the tie and check points used in the geometric integration.

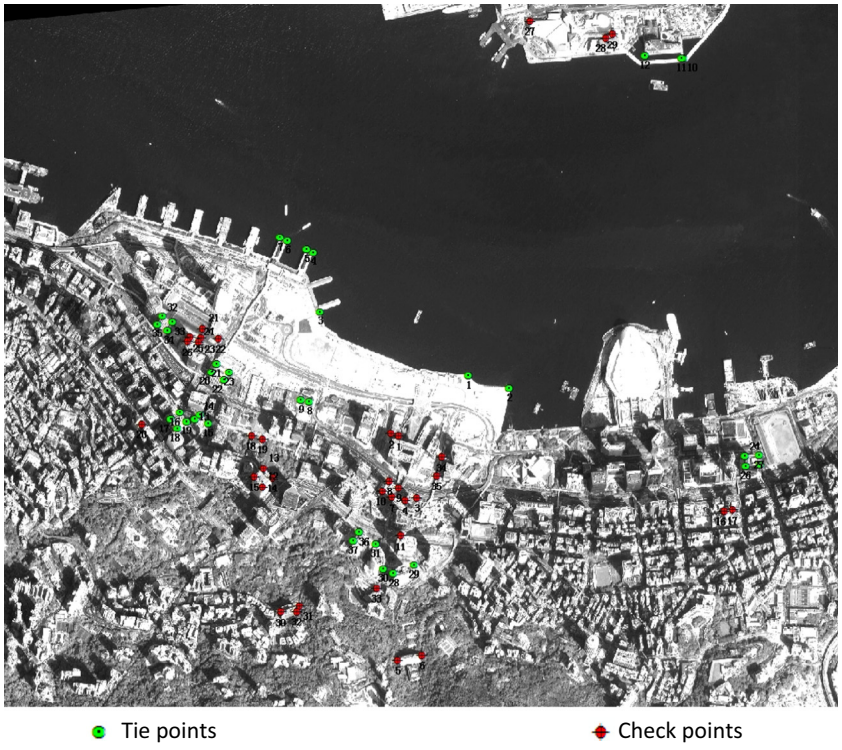

Fig. 7. The Pleiades-1 image of the study area, marked with the tie and check points used in the geometric integration.

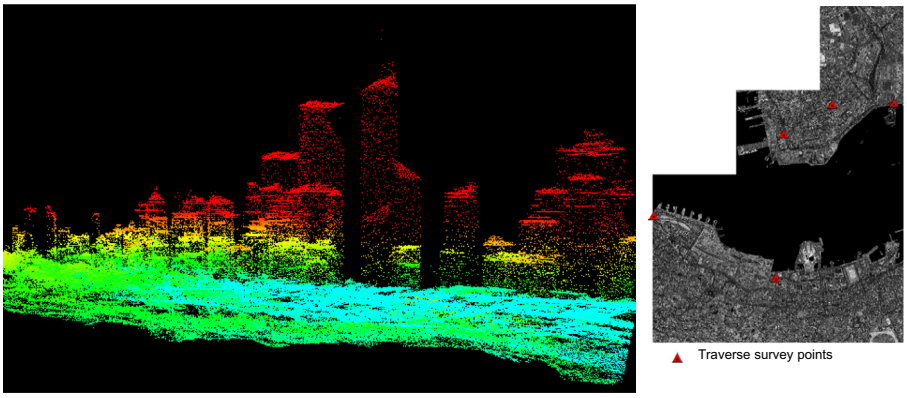

(a) 3D view of partial of the LiDAR points (b) LiDAR intensity map

Fig. 8. LiDAR data of the study area and the distribution of the traverse survey points used to check accuracy.

The vertical accuracy of the LiDAR data is about 10 cm according to the metafile. However, the horizontal accuracy is much worse. The horizontal coordinators of five traverse survey points obtained from the Lands Department of Hong Kong government (http://www.geodetic.gov.hk/smo/gsi/programs/en/traverse_station.asp) are compared with those identified from the LiDAR data. For each traverse survey point, a location map and a station photo are provided and can be used to identify the corresponding point in the LiDAR data by referring to the intensity map. The five traverse survey points are selected because they represent distinct surface features and can be accurately identified in the LiDAR intensity map. They are marked in Fig. 8(b) with triangles. The traverse survey points are accurate to the millimeter. Table 2 lists the detailed comparison results.

5.2. Experimental results for the ZY-3 imagery and LiDAR data

It should be noted that not all of the LiDAR points need to be processed when HRSI and LiDAR data are geometrically integrated. Doing so is not necessary and incurs a calculation cost due to the large volume of data. Instead, a sampling strategy is used to select a reasonable number of points (several hundreds to thousands) from the LiDAR data. These selected LiDAR points should have a similar coverage with the satellite images and are relatively evenly distributed in the area.

The experiment involving the ZY-3 imagery and LiDAR data used 17 vertical tie points and 29 horizontal tie points. To check the results of the geometric integration, 57 check points were identified manually. These check points in the ZY-3 imagery were

feature points with distinct textures. Their 3D coordinates in object space were derived from the adjusted LiDAR data, of which an affine transformation was applied to the original LiDAR data using the five traverse survey points. The accuracy of the adjusted LiDAR data should generally match that of the traverse survey points. Fig. 6 presents the ZY-3 image with the tie point and check point distributions marked.

Table 3 lists the original dominating RPCs of the ZY-3 stereo images and the improved dominating RPCs after the geometric integration process for comparison purposes. All of the 18 dominating RPCs were adjusted during the combined adjustment. Table 3 shows that, generally the dominating RPCs in numerators changed less compared with those in denominators. This indicates that if greater changes applied to the numerators, it will result in greater influences on the geopositioning accuracy of the satellite images, which is consistent with the conclusion that Fig. 1 shows.

The used LiDAR points were back-projected to the ZY-3 stereo images based on their original RPCs to evaluate the effectiveness of the geometric integration. If there was no bias in the original RPCs, the back-projected points on the ZY-3 stereo images should have been homogeneous, representing the same texture features. However, Fig. 9 indicates that this was not the case. In Fig. 9(a), the red crosses are the back-projected points of the LiDAR points on the ZY-3 forward- and backward-looking images. The green intersection signs on the backward-looking image are the homogeneous points of the red crosses on the forward-looking image. As Fig. 9(a) shows, there are discrepancies at the different levels between them. The same used LiDAR points were back-projected to the ZY-3 stereo images based on the improved RPCs after geometric integration. The results are shown in Fig. 9(b), which shows that the discrepancies were effectively removed.

Table 4 lists the statistics of the discrepancies in image space before and after geometric integration for the used 246 LiDAR points, including the RMSE, maximum and minimum of the discrepancies. According to the table, the RMSE of the discrepancies decreased from 5.264 pixels to 0.727 pixels and the maximum decreased from 8.264 pixels to 1.777 pixels after geometric integration. This indicates that the geometric inconsistencies between the ZY-3 imagery and LiDAR data decreased significantly.

The performance of the geometric integration was also examined in object space. The geopositioning accuracies of three methods, including a direct intersection using original RPCs, an affine transformation using several GCPs and the geometric integration solution, were compared using the same 57 check points mentioned previously. The discrepancies (RMSE) in the *X*, *Y* and *Z* directions in object space were calculated by comparing the ground coordinates derived from the three methods with those of the check points. Table 5 presents the results.

As expected, the direct intersection using the original RPCs generated the worst results, as no GCPs were involved. The affine transformation method used eight GCPs and produced better accuracies in all three directions. The geometric integration results were the best. Geometric integration significantly improved the vertical accuracy, which was not improved much by the affine transformation method. The accuracy obtainable from the geometric integration approach for the ZY-3 imagery was about one pixel in size (3.37 m/pixel) in each direction.

The geometric integration improved the geopositioning accuracy of not only the ZY-3 imagery, but also the LiDAR points. In the experiment, only the horizontal coordinates of the LiDAR data were adjusted, as the height information of the LiDAR data was already very accurate. After geometric integration, the horizontal

Table 2
Comparison between the traverse survey points and corresponding LiDAR points.

Traverse survey points			Corresponding LiDAR points		Errors	
ID	*X* (m)	*Y* (m)	*X* (m)	*Y* (m)	*X*-error (m)	*Y*-error (m)
5,142.009	836,890.698	817,845.221	836,892.594	817,846.834	1.896	1.613
5,101.008	835,571.059	817,487.777	835,572.384	817,489.170	1.325	1.393
2,099.014	834,013.325	816,515.356	834,014.902	816,516.815	1.577	1.459
5,059.009	836,148.866	817,837.604	836,150.660	817,838.283	1.794	0.679
2,060.031	835,474.993	815,780.212	835,475.668	815,780.995	0.675	0.783
Average error:					1.453	1.185

Table 3
Comparison between the individual dominating RPCs of the ZY-3 images before and after combined adjustment.

Dominating RPCs		Forward-looking image		Backward-looking image	
		Before integration	After integration	Before integration	After integration
a_1	LINE_NUM_COEFF_1	5.5066E−04	5.4123E−04	−2.0898E−05	−4.5819E−04
a_2	LINE_NUM_COEFF_2	−2.2048E−01	−2.2228E−01	−2.2266E−01	−2.2109E−01
a_3	LINE_NUM_COEFF_3	−1.1472E+00	−1.1482E+00	−1.1476E+00	−1.1469E+00
a_4	LINE_NUM_COEFF_4	6.3823E−03	6.3512E−03	−6.5161E−03	−6.7345E−03
a_5	LINE_NUM_COEFF_5	8.3365E−04	−3.5342E−03	5.8691E−05	4.3807E−03
b_2	LINE_DEN_COEFF_2	3.3061E−04	−5.1636E−03	1.3332E−04	5.4381E−03
b_3	LINE_DEN_COEFF_3	5.8275E−06	−7.8250E−03	−1.5244E−05	8.1964E−03
b_4	LINE_DEN_COEFF_4	2.1853E−05	−1.7326E−03	−7.4503E−07	−1.2698E−03
b_5	LINE_DEN_COEFF_5	4.8014E−06	1.5818E−04	7.4535E−06	−3.3087E−04
c_1	SAMP_NUM_COEFF_1	6.3408E−05	7.6502E−04	6.6157E−05	2.7932E−04
c_2	SAMP_NUM_COEFF_2	1.1756E+00	1.1749E+00	1.1776E+00	1.1781E+00
c_3	SAMP_NUM_COEFF_3	−2.5493E−01	−2.5602E−01	−2.5567E−01	−2.5493E−01
c_4	SAMP_NUM_COEFF_4	8.9609E−06	4.5005E−04	3.7742E−05	−5.8523E−06
c_5	SAMP_NUM_COEFF_5	−2.0383E−04	1.5913E−03	1.3729E−04	−1.6771E−03
d_2	SAMP_DEN_COEFF_2	2.3911E−04	−3.8058E−04	3.5116E−04	8.2400E−04
d_3	SAMP_DEN_COEFF_3	1.9803E−03	3.3331E−04	2.3031E−03	4.3559E−03
d_4	SAMP_DEN_COEFF_4	−9.0511E−04	1.0108E−03	−8.5172E−04	−1.4416E−03
d_5	SAMP_DEN_COEFF_5	−6.1049E−05	−7.2346E−04	−6.1249E−05	4.7095E−04

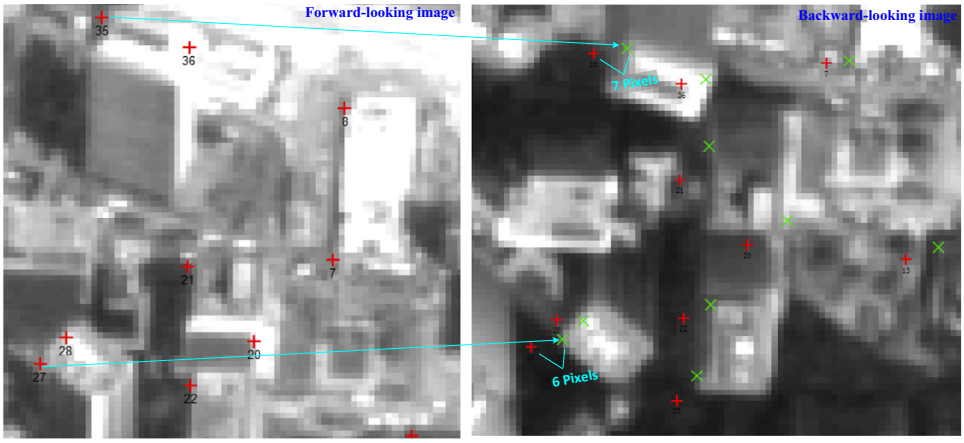

(a) LiDAR back-projected points on the stereo images before geometric integration

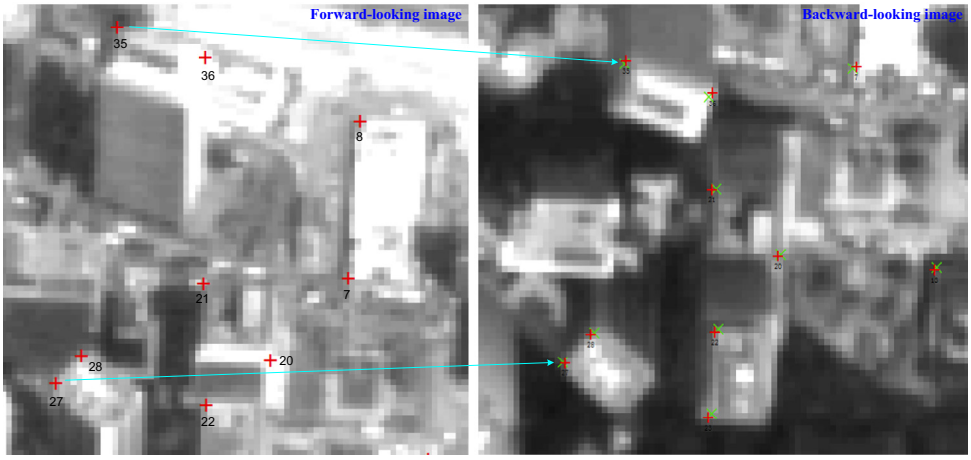

(b) LiDAR back-projected points on the stereo images after geometric integration

Fig. 9. Comparison of the discrepancies in the ZY-3 stereo images.

Table 4
Statistics of discrepancies in image space before and after geometric integration for the ZY-3 imagery.

	Discrepancies	
	Before geometric integration	After geometric integration
Maximum	8.264 pixels	1.777 pixels
Minimum	3.775 pixels	0
RMSE	5.264 pixels	0.727 pixels

Table 5
Geopositioning accuracies of the ZY-3 imagery using three different methods.

Method	RMSE of the discrepancies from the check points		
	σX (m)	σY (m)	σZ (m)
Direct intersection	14.56	7.15	2.87
Affine transformation	4.78	3.68	2.79
Geometric integration	3.95	3.46	2.12

coordinates of the used LiDAR points were refined, and based on those points the entire LiDAR dataset was transferred to a new set using a least squares adjustment approach. The new LiDAR dataset was again compared with the five traverse survey points. Table 6 shows the results.

As Table 6 shows, the horizontal accuracy of the LiDAR data was significantly improved in both the X and Y directions. Geometrically integrating HRSI and LiDAR data to improve the accuracy of the latter has the following merits. First, it enables LiDAR data to be improved without any GCPs. In the experiment, only the five traverse survey points were used as ground truth. However, they were not involved in the geometric integration process. Rather, they were used only to evaluate the accuracy of the LiDAR data and help in the selection of check points. Second, the LiDAR points in the geometric integration were improved on an individual basis, which allowed for different adjustments to be made to individual LiDAR points in different local regions. This could not have been achieved using the general transformation methods based on GCPs, as doing so would have transferred the LiDAR dataset to a whole new set.

5.3. Experimental results for the Pleiades-1 imagery and LiDAR data

The experiment involving the Pleiades-1 imagery and LiDAR data used 12 vertical tie points and 25 horizontal tie points. Thirty-five check points were identified manually to confirm the results of the geometric integration. The distributions of the tie and check points are marked in the Pleiades-1 image shown in Fig. 7.

The performance of the geometric integration approach was initially evaluated in image space. Two hundred and sixty sampled

LiDAR points were back-projected to the Pleiades-1 stereo images based on their original and improved RPCs after geometric integration. Table 7 lists the statistics of the discrepancies for the used LiDAR points in image space before and after geometric integration.

As Table 7 shows, the discrepancies between the original and improved RPCs are better in the Pleiades-1 imagery than in the ZY-3 imagery, perhaps due to the higher accuracy of the original RPCs and higher resolution of the Pleiades-1 imagery. The discrepancies decreased from 2.810 pixels to 0.945 pixels and the maximum decreased from 7.585 pixels to 1.691 pixels after geometric integration.

Table 8 compares the geopositioning accuracies in object space for the three methods. The direct intersection using the original RPCs of the Pleiades-1 imagery generated good results, again verifying the good quality of the original RPCs. The affine transformation method improved the accuracies but not by much in the X and Z direction, and the geometric integration approach notably improved the accuracies in all three directions. The accuracy obtained using the geometric integration approach for the Pleiades-1 imagery was about 2.6 pixels in size (0.5 m/pixel) in each direction.

Table 6
Discrepancies between the traverse survey points and corresponding LiDAR points before and after geometric integration with the ZY-3 imagery.

	Discrepancies	
	Before geometric integration (m)	After geometric integration (m)
Average X-error	1.453	0.37
Average Y-error	1.185	0.54

Table 7
Statistics of discrepancies in image space before and after geometric integration for the Pleiades-1 imagery.

	Discrepancies	
	Before geometric integration	After geometric integration
Maximum	7.585 pixels	1.691 pixels
Minimum	0.856 pixels	0
RMSE	2.810 pixels	0.945 pixels

Table 8
Geopositioning accuracies of the Pleiades-1 imagery using three different methods.

Method	RMSE of the discrepancies from the check points		
	σX (m)	σY (m)	σZ (m)
Direct intersection	1.70	2.26	1.44
Affine transformation	1.53	1.42	1.40
Geometric integration	1.26	1.39	1.36

Table 9
Discrepancies between the traverse survey points and corresponding LiDAR points before and after geometric integration for the Pleiades-1 imagery.

	Discrepancies	
	Before geometric integration (m)	After geometric integration (m)
Average X-error	1.453	0.07
Average Y-error	1.185	0.17

As Table 9 shows, the geometric integration of the Pleiades-1 imagery and LiDAR data significantly improved the horizontal accuracy of the LiDAR data. The Pleiades-1 imagery improved the LiDAR data more than the ZY-3 imagery. The Pleiades-1 imagery offered a better horizontal geopositioning accuracy of about 2 m with the original RPCs than the ZY-3 imagery, which offered an accuracy of about 15 m. The resolution of the Pleiades-1 imagery was about 0.5 m/pixel, much higher than that of the ZY-3 imagery (3.37 m/pixel).

6. Conclusions and discussion

This paper presents a geometric integration model to integrate HRSI and airborne LiDAR data and improve geopositioning accuracy in metropolitan areas. Through theoretical analysis and experimental validation, the following conclusions can be drawn.

(1) The geometric integration model is able to effectively decrease the inconsistencies between HRSI and LiDAR data, and improve the geopositioning accuracies of both datasets.
(2) For ZY-3 imagery, the accuracy obtained after geometric integration can be significantly improved to about one pixel in size (3.37 m/pixel for ZY-3 imagery). For Pleiades-1 imagery, the accuracy obtained after geometric integration can be improved to about 2.6 pixels in size (0.5 m/pixel for Pleiades-1 imagery). The geometric integration method performs better than the traditional affine transformation methods in both cases.
(3) The geometric integration of HRSI and LiDAR data can also improve the accuracy of LiDAR data. The higher accuracy of the original RPCs and higher resolution of the HRSI better the improvements to the LiDAR data.

The geometric integration model discussed here enables the integration of remote sensing imagery and laser scanning data from different platforms and sensors. This encourages a more accurate derivation of consistent 3D spatial information, and permits the full comparative and synergistic use of different datasets from different sources. The geometric integration strategy can also be used in other similar applications such as the integrated processing of close-range images and terrestrial laser scanning data.

Acknowledgements

The authors would like to thank the Hong Kong government's Civil Engineering and Development Department (CEDD) for providing the LiDAR dataset. The work was supported by a grant from the Research Grants Council of Hong Kong (Project No. PolyU 5330/12E) and a grant from the National Natural Science Foundation of China (Project No. 91338110).

References

Adams, J., Chandler, J., 2002. Evaluation of Lidar and medium scale photogrammetry for detecting soft-cliff coastal change. Photogram. Rec. 17 (99), 405–418.
Anderson, F.S., Parker, T.J., 2002. Characterization of MER landing sites using MOC and MOLA. In: Proceedings of the 33rd Lunar and Planetary Science Conference, League City, Texas, March 11–15.
ASPRS, 2014. ASPRS positional accuracy standards for digital geospatial data. Photogramm. Eng. Rem. Sens. 81 (3), 53, <http://www.asprs.org/Standards-Activities.html>.
Baltsavias, E.P., Pateraki, M.N., Zhang, L., Baltsavias, E.P., Baltsavias, E.P., 2001. Radiometric and Geometric Evaluation of Ikonos GEO Images and Their Use for 3D Building Modelling. Citeseer.
Bowen, Z.H., Waltermire, R.G., 2002. Evaluation of Light Detection and Ranging (LiDAR) for Measuring River Corridor Topography. Wiley Online Library.
Croft, J., 2008. Prodigious mapping capabilities, spatial resolution and geo-location ability: GeoEye's next-generation Imaging Satellite. GeoInformatics 4, 18–23.

Csanyi, N., Toth, C.K., 2007. Improvement of Lidar data accuracy using Lidar-specific ground targets. Photogramm. Eng. Rem. Sens. 73 (4), 385–396.
Dial, G., Grodecki, J., 2002. Block adjustment with rational polynomial camera models. In: Proceedings of ASPRS 2002 Conference, Washington, D.C., pp. 22–26.
Di, K., Wang, J., Ma, R., Li, R., 2003a. Automatic shoreline extraction from high-resolution IKONOS satellite imagery. In: Proceedings of ASPRS 2003 Annual Conference. Citeseer.
Di, K., Ma, R., Li, R., 2003b. Geometric processing of Ikonos stereo imagery for coastal mapping applications. Photogramm. Eng. Rem. Sens. 69 (8), 873–879.
Di, K., Hu, W., Liu, Y., Peng, M., 2012. Co-registration of Chang'E-1 stereo images and laser altimeter data with crossover adjustment and image sensor model refinement. Adv. Space Res. 50 (12), 1615–1628.
Fraser, C.S., Hanley, H.B., 2005. Bias-compensated RPCs for sensor orientation of high-resolution satellite imagery. Photogramm. Eng. Rem. Sens. 71 (8), 909–915.
Fraser, C.S., Baltsavias, E., Gruen, A., 2002. Processing of Ikonos imagery for submetre 3D positioning and building extraction. ISPRS J. Photogramm. Rem. Sens. 56 (3), 177–194.
Fraser, C.S., Ravanbakhsh, M., 2009. Georeferencing accuracy of GeoEye-1 imagery. Photogramm. Eng. Rem. Sens. 75 (6), 634–638.
Glenn, N.F., Streutker, D.R., Chadwick, D.J., Thackray, G.D., Dorsch, S.J., 2006. Analysis of LiDAR-derived topographic information for characterizing and differentiating landslide morphology and activity. Geomorphology 73 (1), 131–148.
Habib, A., Shin, S.W., Kim, K., Kim, C., Bang, K., Kim, E.M., Lee, D.C., 2007. Comprehensive analysis of sensor modeling alternatives for high-resolution imaging satellites. Photogramm. Eng. Rem. Sens. 73 (11), 1241–1251.
Habib, A., 2008. Accuracy, quality assurance, and quality control of LiDAR data. In: Shan, J., Toth, C. (Eds.), Topographic Laser Ranging and Scanning Principles and Processing. Taylor & Francis Group/CRC Press, Boca Raton, FL, USA, pp. 269–293, ISBN: 978-1-4200-5142-1.
Hodgson, M.E., Jensen, J.R., Schmidt, L., Schill, S., Davis, B., 2003. An evaluation of LiDAR-and IFSAR-derived digital elevation models in leaf-on conditions with USGS Level 1 and Level 2 DEMs. Remote Sens. Environ. 84 (2), 295–308.
Hladik, C., Alber, M., 2012. Accuracy assessment and correction of a LIDAR-derived salt marsh digital elevation model. Remote Sens. Environ. 121, 224–235.
Kasai, M., Ikeda, M., Asahina, T., Fujisawa, K., 2009. LiDAR-derived DEM evaluation of deep-seated landslides in a steep and rocky region of Japan. Geomorphology 113 (1), 57–69.
Li, R., Deshpande, S., Niu, X., Zhou, F., Di, K., Wu, B., 2008. Geometric integration of aerial and high-resolution satellite imagery and application in shoreline mapping. Mar. Geodesy 31 (3), 143–159.
Li, R., Zhou, F., Niu, X., Di, K., 2007. Integration of IKONOS and QuickBird imagery for geopositioning accuracy analysis. Photogramm. Eng. Rem. Sens. 73 (9), 1067.
May, N.C., Toth, C.K., 2007. Point positioning accuracy of airborne LiDAR systems: a rigorous analysis. Int. Arch. Photogramm. Rem. Sens. Spatial Inform. Sci. 36 (3/W49B), 107–111.
Neumaier, A., 1998. Solving ill-conditioned and singular linear systems: a tutorial on regularization. Siam Rev. 40 (3), 636–666.
Poli, D., Remondino, F., Angiuli, E., Agugiaro, G., 2013. Evaluation of Pleiades-1a triplet on Trento testfield. Int. Arch. Photogramm. Rem. Sens. Spatial Inform. Sci. XL-1/W1, 287–292.
Populus, J., Barreau, G., Fazilleau, J., Kerdreux, M., L'Yavanc, J., 2001. Assessment of the LiDAR topographic technique over a coastal area. In: Proceedings of CoastGIS'01: 4th International Symposium on GIS and Computer Mapping for Coastal Zone Management. CoastGIS, Halifax, Nova Scotia.
Qiao, G., Wang, W., Wu, B., Liu, C., Li, R., 2010. Assessment of geo-positioning capability of high-resolution satellite imagery for densely populated high buildings in metropolitan areas. Photogramm. Eng. Rem. Sens. 76 (8), 923–934.
Sohn, G., Dowman, I., 2007. Data fusion of high-resolution satellite imagery and LiDAR data for automatic building extraction. ISPRS J. Photogramm. Rem. Sens. 62 (1), 43–63.
Spiegel, M., 2007. Improvement of interior and exterior orientation of the three line camera HRSC with a simultaneous adjustment. Int. Arch. Photogramm. Rem. Sens. Spatial Inform. Sci. 36 (3/W49B), 161–166.
Stal, C., Tack, F., Maeyer, P., Wulf, A., Goossens, R., 2013. Airborne photogrammetry and LIDAR for DSM extraction and 3D change detection over an urban area: a comparative study. Int. J. Remote Sens. 34 (4), 1087–1110.
St-Onge, B., Hu, Y., Vega, C., 2008. Mapping the height and above-ground biomass of a mixed forest using LiDAR and stereo IKONOS images. Int. J. Remote Sens. 29, 1277–1294.
Steinmann, K., Mandallaz, D., Ginzler, C., Lanz, A., 2013. Small area estimations of proportion of forest and timber volume combining LiDAR data and stereo aerial images with terrestrial data. Scand. J. For. Res. 28, 373–385.
Tao, C.V., Hu, Y., 2001. A comprehensive study of the rational function model for photogrammetric processing. Photogramm. Eng. Rem. Sens. 67 (12), 1347–1358.
Teo, T., Chen, L., 2004. Object-based building detection from LiDAR data and high resolution satellite imagery. In: Proceedings of Asian Conference on Remote Sensing. Ching-Mai, Thailand (on CD-ROM), pp. 22–26.
Toutin, T., 2006. Comparison of 3D physical and empirical models for generating DSMs from stereo HR images. Photogramm. Eng. Rem. Sens. 72 (5), 597–604.
Tong, X., Liu, S., Weng, Q., 2010. Bias-corrected rational polynomial coefficients for high accuracy geo-positioning of QuickBird stereo imagery. ISPRS J. Photogramm. Rem. Sens. 65 (2), 218–226.
Wang, J., Di, K., Li, R., 2005. Evaluation and improvement of geopositioning accuracy of IKONOS stereo imagery. J. Surv. Eng. 131 (2), 35–42.
Wang, T., Zhang, G., Li, D., Tang, X., Jiang, Y., Pan, H., Zhu, X., 2014. Planar block adjustment and orthorectification of ZY-3 satellite images. Photogramm. Eng. Rem. Sens. 80 (5), 559–570.
Wu, B., Guo, J., Zhang, Y., King, B., Li, Z., Chen, Y., 2011a. Integration of Chang'E-1 imagery and laser altimeter data for precision lunar topographic modeling. IEEE Trans. Geosci. Remote Sens. 49 (12), 4889–4903.
Wu, B., Zhang, Y., Zhu, Q., 2011b. A triangulation-based hierarchical image matching method for wide-baseline images. Photogramm. Eng. Rem. Sens. 77 (7), 695–708.
Wu, B., Zhang, Y., Zhu, Q., 2012. Integrated point and edge matching on poor textural images constrained by self-adaptive triangulations. ISPRS J. Photogramm. Rem. Sens. 68 (2012), 40–55.
Wu, B., Hu, H., Guo, J., 2014. Integration of Chang'E-2 imagery and LRO laser altimeter data with a combined block adjustment for precision lunar topographic modeling. Earth Planet. Sci. Lett. 391, 1–15.
Xhardé, R., Long, B.F., Forbes, D.L., 2006. Accuracy and limitations of airborne LiDAR surveys in coastal environments. 2006 International Geoscience and Remote Sensing Symposium. IEEE, Denver, CO, pp. 2412–2415.
Yoon, J., Shan, J., 2005. Combined adjustment of MOC stereo imagery and MOLA altimetry data. Photogramm. Eng. Rem. Sens. 71 (10), 1179–1186.